Journal of the Indian Institute of Science
A Multidisciplinary Reviews Journal
ISSN: 0970-4140 Coden-JIISAD

REVIEWS

Advances in Image Reconstruction Methods for Real-Time Magnetic Resonance Thermometry

Jaya Prakash[†], Nick Todd[‡] and Phaneendra K. Yalavarthy[†,]*

Abstract | Magnetic Resonance Imaging (MRI) has been widely used in cancer treatment planning, which takes the advantage of high-resolution and high-contrast provided by it. The raw data collected in the MRI can also be used to obtain the temperature maps and has been explored for performing MR thermometry. This review article describes the methods that are used in performing MR thermometry, with an emphasis on reconstruction methods that are useful to obtain these temperature maps in real-time for large region of interest. This article also proposes a prior-image constrained reconstruction method for temperature reconstruction in MR thermometry, and a systematic comparison using *ex-vivo* tissue experiments with state of the art reconstruction method is presented.

Keywords: *HIFU, MRgHIFU, image reconstruction, temperature maps.*

1 Introduction

Magnetic Resonance Imaging (MRI) provides invaluable visualization of anatomical structures and tumors for treatment planning.[1] It has the capability of providing high-resolution images of soft tissues. In recent years, it has been shown that various MR parameters like T_1-weighted, T_2-weighted, proton density and Proton Resonant Frequency (PRF) can be used to obtain temperature maps distribution, which in turn could be used for thermotherapy. Note that T_1-weighted and T_2-weighted images are obtained due to the variation in the temperature in soft tissue, as a result direct reconstruction of temperature maps could be performed. Thus MRI can be used to obtain temperature distribution during thermal treatment (thermotherapy).[2]

Many thermal therapies are prelevant, the most famous ones use focused ultrasound (FUS) or laser inducer interstitial thermotherapy (LITT).[3] In LITT, a laser light produced by Nd:YAG laser having a wavelength of 1064 nm is used, the laser light is absorbed and converted to heat, which causes change in the optical properties of the tissue leading to coagulation (thermal damage to proteins). This culminates in killing of cancerous tissues.[4] It is a minimally invasive technique, where a fiber optic cable carrying laser light is used with a diffusive tip to deposit energy precisely at the region of interest.[3] As the fiber optic tip is quite small, it can only be used for treating small tumors,[3] making it not ideal for treating large tumors. Usage of laser does not interfere with MR measurements, hence MRI can be used to obtain the k-space (Fourier) measurements while preforming thermotherapy using LITT. These recorded MRI measurements can be used in turn to obtain the temperature distribution at the region of interest. MR guided LITT (MRgLITT) was successfully used for treatment on various organs like brain, liver, bone and prostrate.[5]

Focused Ultrasound Surgery (FUS) or High-intensity Focused Ultrasound (HIFU) is an efficient noninvasive technique to treat patients having cancerous tumors.[6,7] HIFU has been used extensively for treating breast tumors, uterine fibroids and brain lesions.[8] One of the major advantage of HIFU is its ability to focus on the tumor site (highly localized), which is not possible with radiation therapy, hence making HIFU prone to lesser side effects. Note that both diagnostic ultrasound and therapeutic ultrasound uses sound waves in different frequency range to create the required effect (diagnose abnormality or treat tumor).

[†]Supercomputer Education and Research Centre, Indian Institute of Science, Bangalore 560012, India.
[‡]Institute of Neurology, Faculty of Brain Sciences, University College London, London, United Kingdom.
**phani@serc.iisc.in*

The frequency of sound waves used in diagnostic ultrasound depends on the depth you need to image (region of interest). The typical frequency range used is 3–10 MHz (> 20 MHz for skin scan).[9] While in therapeutic ultrasound, i.e. in HIFU, the frequency range used is in the order of 1–2 MHz.[10] The most important aspect in HIFU treatment is that focusing of ultrasound beam at the tumor site leads to a temperature rise at the focal spot. This rise in temperature results in breakage of cell walls of tumor cells hence destroying the cells at the focal spot. The typical power output generated by diagnostic ultrasound is less than 5 mW/cm^2, while it is greater than 100 mW/cm^2 in therapeutic ultrasound.[8,11]

MR guided HIFU (MRgHIFU) and MRgLITT uses same MR physics to estimate the temperature distribution. The basic idea in obtaining the temperature distribution from T_1-weighted and T_2-weighted MR images is that the relaxation times used to obtain T_1-weighted and T_2-weighted MR images are affected by the temperature of the soft tissues.[12] The change in relaxation time (used for T_1- and T_2-weighted images) is due to spin-lattice relaxation present in the biological tissues.[13,14] This relaxation occurs due to the dipole interaction of macromolecules and water molecules, which is observed mainly due to rotational and translational motion.[14,15] A rise in temperature will effect this motion leading to change in relaxation time, and hence changes will be reflected in the T_1- and T_2-weighted contrast.[14,15] When Proton Resonance Frequency (PRF) is the MR parameter, the rise in temperature at resonant frequency has a direct correlation to the change in phase of the recorded MR data.

The PRF contrast can also be used for estimating the temperature distribution.[16] The MR signal frequency depends on the chemical environment of water hydrogen, increase in temperature changes this environment, which helps in measuring the temperature change.[16] A hydrogen atom contains protons which is shielded by electron, leading to a reduction in the resonant frequency.[16,17] Hence in water molecule, the electron in the hydrogen atom is pulled by the bond between hydrogen and oxygen molecule resulting in increase in resonant frequency. An increase in temperature will twist, stretch and break the bond between hydrogen and oxygen atom.[16,17] This leads to a modest increase in electron shielding of the hydrogen proton from the magnetic field, leading to a reduction in the net field observed by the proton and hence changes the overall resonant frequency. Using PRF parameter, it can be shown that a phase change will directly correspond to temperature change.[16–18]

Obtaining high spatial-, temporal resolution, and volume coverage at the region of interest (hotspot) is a challenge in MR temperature imaging.[8] Temperature rise of several degrees of centigrade per second over a volume of few millimeter can be achieved by inducing a HIFU sonification.[8] High spatial and temporal resolution for monitoring these rapid temperature changes is essential, currently a 2-D imaging sequence with just a few slices covering the hotspot is used. Transcranial MRgHIFU applications require optimal monitoring of three-dimensional (3D) temperature maps with large volume coverage and high spatio-temporal resolution for accurate tracking of rapid heating at the focus and monitoring the heating at the near- and far-fields of the ultrasound beam.[19,20] The most critical part of obtaining the temperature map using MRgHIFU is in reconstructing the temperature maps in real-time. Real-time imaging can be possible by reducing the MR scan time and performing faster temperature map reconstruction from the acquired MR data. To achieve real-time therapeutic imaging, advanced image reconstruction methods (based on compressive sensing) can be used, wherein the temperature maps estimation can be performed with lesser measurements, which inturn can lead to faster scan times.[21]

Current state of the art MR temperature map reconstruction techniques in MRgHIFU are using Model Predictive Filtering (MPF),[22] Temporally Constrained Reconstruction (TCR),[21] and parallel imaging with UNFOLD.[23] Model predictive filtering requires prior knowledge about tissue acoustic and thermal properties for accurate estimation of temperature maps.[22] This method uses Pennes bioheat equation as a model along with tissue acoustic properties to obtain the temperature distribution.[22] Both MPF and parallel imaging with UNFOLD methods are not able to monitor the entire 3D volume of interest. Currently, TCR is the only established method that has the ability to provide large coverage 3D temperature measurements.[24] TCR was able to achieve accurate temperature measurements with $1.5 \times 1.5 \times 3.0$ mm spatial resolution, 1.7 s temporal resolution, and $288 \times 162 \times 78$ mm volume coverage. A major limitation of TCR method was its inability to perform real-time temperature map reconstruction and was therefore limited to retrospective applications.

The usage of Graphics Processing Units (GPUs) was previously explored for performing back-

projection type image reconstruction in cone-beam CT (CBCT) in real-time.[25] Iterative image reconstruction algorithms for CT (voxel driven), which requires scatter and gather operations are performed on GPU, similar kind of algorithms are proposed for PET and SPECT (line driven) and shown to provide good speedups.[25] Similarly, GPU has also been used for acceleration of MRI image reconstruction, where the reconstruction is performed using a simple fast Fourier transform (FFT) from the MRI pulse sequence. These MRI image reconstructions are performed using optimized GPU implementation of FFT known as CUFFT provided by CUDA[26] to advance MRI reconstruction schemes like parallel imaging combined with reconstruction based on conjugate gradient solver.[27] GPU has been explored even in non-linear image reconstruction schemes like diffuse optical tomography,[28] and bioluminescence tomography,[29] which require matrix inversion operations, while fluorescence molecular tomography imaging scheme was parallelized using an open-source software called AGILE.[30] The TCR algorithm (later explained elaborately in this review) implementation in GPU hardware can provide the required acceleration to perform real-time temperature map reconstruction.

The TCR algorithm gives reasonably accurate reconstruction with 2 to 6 times (17–50 %) reduction factor in the k-space (acquired) data, but it does not provide the high level of optimization that is required, especially if the desirable compressed data is around 12 times (8%). Recent works in dynamic Computed Tomography (CT) has shown that better utility of prior image can result in better reconstruction with relatively less number of projection using a Prior Image Constrained Compressive Sensing (PICCS) image reconstruction.[31,32] It is important to note that in CT high under-sampling will help in reduced dosage, while in MRI it helps in faster scan times (desirable in real-time temperature monitoring). Hence, usage of a variant of PICCS as Prior Image Constrained Image Reconstruction (PICIR) algorithm is seen to provide accurate reconstruction with less number of MR measurements.

This review elaborates various MR methods that can be used in providing temperature maps. Further, it introduces various existing state-of-art image reconstruction algorithms for MR thermometry and lists the advantages and disadvantages of each one. Later part of the review explains the PICIR-type image reconstruction and real-time TCR (RT-TCR) based temperature map reconstruction. The comparison with TCR algorithm with these methods is also provided through numerical and *ex-vivo* tissue experiments. Lastly, a brief write-up on future directions in MR temperature imaging is presented.

2 MR Temperature Imaging Methods

This section reviews various ways of estimating temperature distribution using different MR parameters like T_1-weighted, T_2-weighted, proton density, diffusion coefficient and proton resonant frequency.

2.1 *Temperature imaging using T_1-weighted MR images*

Noninvasive temperature monitoring can be performed as relaxation times are function of time.[12] The longitudinal relaxation time refers to the T_1-weighted image. In the early 80's Parker et al. investigated the relation between temperature and longitudinal relaxation rates, given using the following relation[14,15]

$$\frac{1}{T_1} = \frac{\gamma^2 H^2 \tau_0}{1 + \omega_o^2 \tau_o^2} \tag{1}$$

where γ is the gyromagnetic ratio, ω_0 the Larmor frequency, H the local magnetic field induced by local magnetic moments, and τ_0 is the molecular position correlation time. The molecular position correlation time is dependent on temperature via the following relationship,[14,15]

$$\tau_0 = \frac{constant \times \eta}{T} \simeq \frac{K}{T} \tag{2}$$

where K can be considered as a constant (since the viscosity (η) of water changes very less with temperature) and T represents the temperature. A linear behavior between the T_1 contrast and temperature T was observed experimentally, and hence heuristically linear relationship was assumed.[14,15]

More recent works indicate that an increase in temperature leads to a change in the translational and rotational motion.[33] It is well known that the spin-lattice relaxation in biological tissues is observed as a result of bipolar interaction of macromolecules and water molecules which in turn depends on their translational and rotational motion. Hence, an increase in temperature is reflected in longitudinal relaxation (T_1) time. The mathematical model that describes this variation is given as,[14]

$$T_1 \propto e^{\frac{-E_a(T_1)}{kT}} \quad (3)$$

where $E_a(T_1)$ is the activation energy of the relaxation time, k is the Boltzmann constant and T the absolute temperature.[33] Using the above model, Bottomley et al. showed that T_1 contrast has a linear relationship with the temperature ($T_1 \propto \frac{1}{T}$), the same was proved using the dependence on relaxation time. The temperature depends linearly with the longitudinal relaxation time (T_1 contrast). But the contrast is also affected by the tissue type, given by[39]

$$T_1(T) = T_1(T_{ref}) + m(T - T_{ref}) \quad (4)$$

where T_{ref} is the reference temperature and $m = \frac{dT_1}{dT}$, which is estimated empirically for various tissues.[34] Typical values of T_1(T) is 1.4%/°C for bovine muscle,[35,36] 0.97%/°C for fat,[37] and 1–2%/°C for liver.[38,39]

The relation between the repetition time (TR), reference temperature (T_{ref}), flip angle (α), m, and T_1 contrast is given by temperature sensitivity ($\frac{dS}{SdT}$) as[40]

$$\frac{dS}{SdT} = \frac{m\,TR(1-cos(\alpha))E_1}{T(T_{ref})^2(1-E_1)(1-cos\,\alpha\,E)} - \frac{1}{T_{ref}} \quad (5)$$

where S and E_1 is given by[39,40]

$$S = M_0\ sin(\alpha)\frac{1-E_1}{1-cos(\alpha)\,E_1} \quad (6)$$

$$E_1 = \exp\left(-\frac{TR}{T_1(T_{ref}) + m(T - T_{ref})}\right) \quad (7)$$

with M_0 representing the equilibrium magnetization. Note that the accuracy of MR temperature imaging depends on the accuracy of measuring and estimating the T_1-weighted contrast. Presence of lipids leads to artifacts in the T_1-weighted images, and hence cannot be used for MR thermometry; this can be overcome by using lipid suppression techniques.[39] Obtaining accurate T_1-weighted images can be done using inversion recovery methods, but these tend to be computationally expensive. Hence T_1-weighted methods are always used with multiple readout pulses (multiple slices are acquired simultaneously), making it more suitable for hyperthermia applications.[41] The above equations contain a coefficient (m, which is tissue dependent), typically this coefficient is not known for individual tissue type, and hence T_1-weighted measurements have a drawback of not providing quantitative temperature maps during heating. Most T_1-weighted temperature map imaging are used in situations where rapid qualitative imaging is sufficient.[42]

2.2 *Temperature imaging using T_2-weighted MR images*

The transversal relaxation time (T_2) follows a similar trend of a T_1 relaxation time. The variation of T_1- and T_2-weighted contrast with exponential time constant of autocorrelation function is given as[43,44]

$$\frac{1}{T_1} = \frac{A}{5}\left(\frac{\tau_c}{1+(\omega_L\tau_c)^2} + \frac{4\tau_c}{1+(2\omega_L\tau_c)^2}\right) \quad (8)$$

$$\frac{1}{T_2} = \frac{A}{10}\left(3\tau_c + \frac{5\tau_c}{1+(\omega_L\tau_c)^2} + \frac{2\tau_c}{1+(2\omega_L\tau_c)^2}\right) \quad (9)$$

where A is a constant, τ_c is approximately the average time required for a molecule to orient itself through solid angle of 1 degree, and ω_L is the resonant frequency. The above equations can be rewritten as[43]

$$T_1 = T_2 \propto \frac{1}{\tau_c};\ \omega_L\tau_c << 1\ \&\ \tau_c = \tau_0\ exp\left(\frac{E_a}{kT}\right) \quad (10)$$

where $\tau_o = T_1 ln(2)$. Hence, the temperature depends linearly with both T_1 and T_2-weighted contrast until some condition ($\omega_L\tau_c << 1$) holds, a decrease in temperature (from a very high temperature value) will result in a decrease in contrast in this region. When $\omega_L\tau_c >> 1$, then $T_1 \propto \omega_L^2\tau_c$, leading to further decrease in temperature (increase in the T_1-contrast).[43] Therefore, this variation looks like a parabola having a minimum T_1 contrast at $\omega_L\tau_c \approx 0.612$, while a decrease in temperature will result in increase in the value of τ_c. In case of T_2-weighted temperature imaging, the T_2-contrast increases with an increase in the temperature until $\tau_c < T_2$.[43] But when $\tau_c < T_2$ condition is not satisfied (at very low temperatures), T_2-contrast tends to remain a constant as this situation resembles a solid body in the Nuclear Magnetic Resonance (NMR) spectrum, the change in T_2-contrast with temperature follows a sigmoidal increase.[45] A more elaborate discussion and derivation can be found in Freude's lectures.[43]

Previous works have reported that T_2 contrast increases with increase in temperature in aqueous solution. The T_2 contrast for the water in the tissue is lower by a significant factor when compared to pure water. But as already discussed, a reduction in temperature will cause increase in T_2 signal, and an increase results in lower T_2 signal value,[45] this observation has been used

for identifying irreversible tissue damage during thermal coagulation.

The relationship between the Signal to Noise Ration (SNR) and MR parameter is given as[43]

$$SNR \propto \mathcal{N} \gamma^{\frac{5}{2}} B_0^{\frac{2}{3}} T^{-\frac{3}{2}} I(I+1) \sqrt{\frac{T_2}{T_1}} \sqrt{t_{meas}} \qquad (11)$$

where N is the density of nuclei, B_0 the external magnetic field, T represents the absolute temperature, I the nuclear spin, and t_{meas} the measurement time. It can be observed that the SNR depends on the absolute temperature and the contrast (T_1- or T_2-relaxation times). The measurable power in the Radio-Frequency (RF) coil is proportional to the resonant frequency ($\omega_L \propto \gamma B_0$), hence the power of RF coils can be related to the SNR.[43] The electronic noise is observed due to the frequency and the temperature which is given by $\sqrt{\omega T}$, this is also called as white noise.[43] Note that the SNR definition is the same for both T_1- and T_2-weighted temperature imaging. T_2-weighted temperature measurements in case adipose tissues are shown in Ref. 46. As with the T_1-weighted, the temperature maps obtained through T_2-weighted are qualitative in nature, making them not ideal for MR thermometry.

2.3 *Proton density based temperature imaging*

MR signal in proton density weighted imaging is proportional to the number of spinning protons present in the region of interest. The is achieved by having a very long Repetition Time (TR) and Echo Time (TE) being very short, leading to minimal weighting of the relaxation time, thus obtaining a proton density contrast. The temperature can also be measured by measuring the proton density (PD). The proton density linearly depends on the equilibrium magnetization (M_0)[47]

$$PD \propto M_0 = \frac{N\gamma^2 h^2 I(I+1) B_0}{3\mu_0 kT} = \chi_0 B_0 \qquad (12)$$

where N represents the spins per volume and h is the Planck's constant. The susceptibility (χ_0) is related to the absolute temperature (T) as,

$$\chi_0 \propto \frac{1}{T} \qquad (13)$$

Hence, proton density can be used to estimate the temperature changes, for example the equilibrium magnetization change by a factor of −0.30 ± 0.01%/°C between 37°C to 80°C.[48] It is important to note that tracking a change of −0.3%/°C necessiates high SNR, typically a temperature sensitivity of 3°C can be achieved by having an SNR of 100.[49] As already seen, the T_1-weight effects the temperature measurements, to avoid the effect of T_1 on temperature measurement the repetition time of pulse sequence has to be increased in the order of 10 seconds. This restricts the usage of this method for retrospective applications.[50]

Proton density (PD) MR parameter was used in many clinical scenarios, for instance PD was used for performing follow up scan after performing MR guided therapy.[51] Proton density based temperature imaging was used for measuring temperature changes in *ex-vivo* tissue samples like fat[49] Variation of proton density with temperature was studied for adipose and muscle tissues.[52] A decrease in PD was observed in the muscle tissue as temperature increased, but in adipose tissue the PD was found to increase initially as the temperature rose to 50°C, and then decrease as the temperature further increased.[52]

2.4 *Diffusion based temperature imaging*

In here, the MR parameter that is being used for measuring temperature is the diffusion coefficient via spin-echo sequence. The diffusion coefficient explains the thermal Brownian motion of the ensemble of molecules in the tissue, this motion occurs due to temperature variations in the tissue. The temperature is related to diffusion coefficient using the following relation[53]

$$D \approx e^{-\frac{E_a(D)}{kT}} \qquad (14)$$

where $E_a(D)$ indicates the activation energy of molecular diffusion of water. The variation of temperature with diffusion coefficient is given by

$$\frac{dD}{DdT} = \frac{E_a(D)}{kT^2} \qquad (15)$$

This MR parameter can estimate a temperature change of about 2%/°C. The change in temperature can be derived as[54]

$$\Delta T = T - T_{ref} = \frac{kT_{ref}^2}{E_a(D)} \left(\frac{D - D_{ref}}{D_{ref}}\right) \qquad (16)$$

where D and D_{ref} indicates the value of diffusion coefficient at temperature T and T_{ref} (reference temperature) respectively, this result assumes that $\Delta T << T_{ref}$ and that E_a is independent of T.

Note that the above equation shows that measuring temperature using diffusion coefficient does not depend on the magnetic field strength. This kind of measuring temperature was used for non-invasively measuring temperature in-vivo.[55] One of the major advantages of this method is its high temperature sensitivity, but this scheme suffers to provide real-time imaging as the acquisition time is very long (longer echo time required), and hence tends to be extremely sensitive to motion.[55,56] Methods like single-shot Echo Planar Imaging (EPI)[55] and line-scanning[56] techniques have been used to overcome the limitations of long acquisition time and motion artifacts. Another major disadvantage of this method is that temperature dependence on diffusion coefficient becomes non-linear when the tissue conditions change. The diffusion coefficient depends on the amount of water content, the movement of water is affected by proteins, membranes etc. Thermal heating may lead to protein coagulation, and hence avoid movement of water resulting in different diffusion coefficient estimates. The lipid suppression in tissue containing fat has to be incorporated for using diffusion coefficient for estimating temperature maps, as variation in fat results in variation in diffusion coefficient with an increase in temperature.[39] Previous works have used diffusion weighted MRI for early detection of regional cerebral ischemia in cats,[57] and later works have used EPI-diffusion coefficient weighted MR (lesser sensitive to motion) for non-invasive temperature monitoring in acrylamide gel materials, and in-vivo in canine brain tissue.[58]

2.5 *Proton resonance frequency based temperature imaging*

Proton Resonant Frequency (PRF) was seen to be sensitive to temperature during the late 1960's,[13,59] and it was used for spectroscopy and then for MR temperature imaging. Water molecules contain two hydrogen atoms and an oxygen atom, the electron in the hydrogen atom is pulled by the bond between hydrogen and oxygen molecule, resulting in increase in resonant frequency.[16–18] This bond will twist, stretch and break with the increase in temperature.[13,16,60] Increase in temperature will lead to electron shielding of the hydrogen atom from the magnetic field, thereby reducing the net field observed by the proton. This will change the overall resonant frequency, which can act as a signal for MR temperature imaging.

The resonant frequency of the hydrogen atom is due to the presence of the local magnetic field. The field at the nucleus is given by[16]

$$B_{local} = B_0 - B_{0s} = (1-s)B_0 \tag{17}$$

where B_{local} is the local magnetic field, B_0 is the applied magnetic field, and s is the shielding constant or screening constant (dependent on the chemical environment). The resonant frequency now becomes,

$$\omega = \gamma B_{local} = \gamma B_0 (1-s) \tag{18}$$

this shielding constant depends on the temperature, hence proton resonant frequency can be used to estimate the temperature maps. The relationship between shielding constant s and temperature T is given as,

$$s(T) = \alpha T \tag{19}$$

where α indicates some constant, hence the variation of temperature leads to linear variation in shielding constant. Temperature map estimation using PRF shift can be done in two ways, spectroscopic imaging and phase mapping methods.

2.5.1 Spectroscopic imaging using PRF shift:

Proton spectroscopic imaging used for temperature imaging utilizes temperature induced water proton chemical shift. The frequency shift is computed using MR spectra, the shift is measured between water peak and reference peak (this peak remains constant with temperature), the model given in Eq. 18 is used to obtain the temperature map. Absolute temperature imaging is possible as the reference temperature does not get affected by field drift and motion during scan,[61] hence absolute temperature imaging has been demonstrated in human brain.[62]

A spatial resolution of 3–4 mm was achieved by spectroscopic imaging, also the reconstruction of absolute temperature was performed within 1 minute. Various kinds of data acquisition methods have been proposed for spectroscopic imaging, mainly used ones are Echo Planar Spectroscopic Imaging (EPSI), MR Spectroscopic Imaging (MRSI) and Line Scan Echo Planar Spectroscopic Imaging (LSEPSI).[63] This method is used only for retrospective application due to its limitations to achieve high spatial and temporal resolution.[63,64] A thorough study of the effect of MRSI with shimming, eddy currents, spatial localization and post-processing methods has been given by Drost et al.[65] MRSI was used for measuring brain temperature, this helped in studying a variety of clinical conditions such as stroke, traumatic brain injury, and schizophrenia.[66]

2.5.2 Phase mapping using PRF shift: Phase mapping using PRF shift is a widely used imaging technique for obtaining the temperature maps. In this kind of temperature imaging, the phase image of the tissue before the heating is subtracted with the current on (after heating starts) to obtain the temperature distribution. As already described, the phase difference is proportional to the temperature-dependent PRF change and the echo time, the change in temperature is given as,[16]

$$\Delta T = \frac{\phi(T) - \phi(T_0)}{\gamma \alpha B_0 TE} \tag{20}$$

where $\phi(T)$ indicates phase of the current image (data obtained after heating starts), $\phi(T_0)$ is the phase before the heating has started, B_0 is the magnetic field strength and echo time is indicated as TE.

The Gradient Echo (GRE) signal intensity decreases exponentially with increase in TE having a time constant T_2^*. The signal to noise ratio depends on the echo time and can be derived to be[39]

$$SNR \propto TE e^{-\frac{TE}{T_2}} \tag{21}$$

Here an optimal TE can be estimated to obtain a maximum SNR. Hence, differentiating the above equation with respect to TE and equating it to 0 results in obtaining optimal TE as $TE = T_2^*$.[63,67] A variety of effects like tissue type, electrical conductivity, external field shift and susceptibility which influence temperature measurements using proton resonant frequency shift is explain in greater detail by Rieke et al.[39] This scheme is widely used in MRgHIFU for treating brain and breast tumors. The phase mapping using PRF shift is utilized in all discussed image reconstruction algorithms in this review.

3 Image Reconstruction in MR Thermometry

High spatial and temporal resolution of temperature maps is one of the key requirement in in MRgHIFU. High spatial resolution is required while treating organs like breast to avoid temperature measurement errors due to partial volume effect.[68] Increase in spatial resolution accommodates small and non-uniform shaped structures at the focal zone. Typical focal zone using HIFU is 13 mm × 2 mm, the power deposited by using the ultrasound beams follows a Gaussian profile, and working with voxel size larger than 1–2 mm^3 induces errors in temperature measurements due the averaging effects of the Gaussian.[68]

High temporal resolution is another essential aspect in MR thermometry, which enables minimizing the treatment time and better control of HIFU heating. Most important aspect is to know the end point of temperature heating (15–20°C above the body temperature), at which the tissue becomes necrosed.[68] Not exceeding this target temperature is essential, as exceeding this temperature will lead to excessive heating in the near field of ultrasound beam.[68] Excessive heating typically requires more time for cooling, hence an increase in total time of MRgHIFU therapy.[68,69] Fast scan time is also essential as the temperature in the region of interest can rise at a rate of 3°C/sec and the thermal dose is known to double for every 1°C.[68,70] Hence to obtain accurate temperature maps, the reconstruction algorithms should be able to provide high spatial and temporal resolution with less number of measurements (k-space lines) alongwith imaging the entire Field of View (FOV) covering the full anatomy that is being treated.[68] There are many reconstruction methods available for performing temperature map reconstruction in MR thermometry, like solving the Pennes bioheat equation by Model Predictive Filtering (MPF), using parallel imaging with Unaliasing by Fourier-encoding the overlaps using the temporal dimension (UNFOLD), and Temporally Constrained Reconstruction (TCR). These are described in details in the subsequent sections.

3.1 *Model predictive filtering (MPF)*

MPF uses a thermal model (Pennes bioheat equation), which is identified before the therapy begins. The temperature at next time points are predicted based on this temperature model, and this is used to create an estimate of the current k-space data.[68] The temperature at the current time point is estimated using the updated k-space data and a combination of the estimated current k-space data and the acquired undersampled k-space data. The thermal model is based on Pennes bioheat equation given by[22]

$$\rho C \frac{\partial T}{\partial t} = k\nabla^2 T - WC(T - T_{blood}) + Q \tag{22}$$

where T is the temperature of the tissue, ρ the tissue density, k the thermal conductivity of the tissue, C the specific heat of the tissue, Q the deposited power density, and W is the Pennes perfusion parameter. Assuming that the specific heat of the blood and tissue is the same, the values for ρ and C can be considered as 1000 kg/m^3 and 4186 $J/kg/°C$.[68] The other parameter in the model like k, W, and Q are estimated before therapy using low

power continuous pulse and fully sampled k-space data during the heating and cooling phase. Note that the dimensionality of W and Q is same as that of the obtained MR data.

The volume is assumed to be homogeneous and thermal properties are assumed to be isotropic while estimating the parameters (W and Q). The parameter Q is estimated using pixel by pixel linear fit to the first two or three points of the temperature-time curves,[22,68] this parameter estimation assumes that the perfusion and diffusion is negligible for small duration at the start of ultrasound heating. The scalar k (thermal conductivity) is estimated based on measured rate at which the Gaussian-shaped temperature profile of the sample spreads in the direction perpendicular to the ultrasound beam during cooling.[22,68] Using this k, the W can be estimated numerically, at the beginning of cooling period, where Q is zero, via the relation[22]

$$W = \frac{1}{T}\left(\frac{k}{C}\nabla^2 T - \rho\frac{\partial T}{\partial t}\right) \quad (23)$$

The temperature at $n+1$ time frame can now be estimated using the Pennes bioheat equation,[22]

$$T_{n+1} = T_n + \left(\frac{k}{\rho C}\nabla^2 T_n - \frac{W}{\rho}T_n + \frac{u_n}{\rho C}Q_{rel}\right).\Delta t \quad (24)$$

where Q_{rel} is the normalized power distribution, u_n is the ultrasound power applied at n^{th} time frame, and Δt is the time step. The spatial derivative (∇^2) can be calculated numerically for each pixel. The first time frame of the acquired k-space data must be fully sampled.[68] The next time frames can be sampled by a undersampling factor of S. The important steps in recursive model predictive filtering algorithm are[22,68]

1. With the current temperature estimate at time n as T_n, acquire the undersampled k-space data at time frame $n+1$.
2. Use the thermal model given by the bioheat equation, estimate the new temperature T_{n+1} at $n+1$ time frame using Eq. 24.
3. Create a complex image at time frame $n+1$ using the magnitude of image at n^{th} time frame and calculate the phase $\phi(n+1)$ as, $\phi(n+1) = \phi(n) + \gamma B_0 \alpha TE(T_{n+1} - T_n)$; $\alpha = -0.01 ppm/°C$.
4. This complex image is projected to k-space by taking a Fourier Transform.
5. The acquired undersampled data at time n+1, is filled with the corresponding predicted lines.
6. This updated k-space data is transformed to image space using inverse Fourier Transform and a new temperature distribution is estimated.

It can be seen that the above algorithm provides a very good resolution, but has an inherent drawback of requiring to estimate many parameters like α, W, Q, k, and C.[22] These parameters are generally tissue dependent, making this process computationally intensive task. But MPF based algorithm was shown to work well in presence of motion, due to inclusion of motion detection and correction steps into the algorithm.[68] More details about MPF can be found in Ref. 22.

3.2 *Parallel imaging with UNFOLD*

This reconstruction technique assumes that thermal therapy takes place on much smaller Field of View (FOV) than the entire organ, thereby providing faster temperature imaging. Fast imaging strategies like two-dimensional spatially-selective RF (2DRF) excitation, unaliasing by Fourier encoding of the overlaps using the temporal dimension (UNFOLD), and parallel imaging are combined. The assumption is that 2DRF excitation approach is well-suited for temperature monitoring, as larger FOV is required to avoid aliasing, which is often substantially larger than the heated volume. The UNFOLD and parallel imaging techniques can be used to remove the aliasing artifacts introduced by 2DRF excitations, and enable use of shorter 2DRF pulse durations (thereby providing real-time imaging capability).

This algorithm assumes that the only a small part of the FOV is to be imaged and the Signal to Noise Ratio (SNR) is not a limiting factor.[71] With these assumptions, the data is collected pertaining to this small FOV by acquiring fewer k-space lines, leading to faster acquisition time.[71] This kind of data collection leads to aliasing artifacts from signal outside the FOV, this could be overcome by using a 2DRF pulse to limit the excitation of the desired region of interest in the phase encoding direction.[23] A RF field is a composition of multiple sub pulses weighted with k-space weighting function, magnetic field gradient and the excitation profile. The excitation profile $M(r)$ can be expressed as,[23]

$$M(r) = i\gamma M_0 \int W(k)S(k)exp(ir.k)\,dk \quad (25)$$

where r and k are vectors. Here M_0 indicates the original longitudinal magnetization, $S(k)$ is the

sampling function of the excitation k-space, $W(k)$ is the weighting function, and $k(t)$ is given as[23]

$$k(t) = -\gamma \int_t^T G(\tau)\, d\tau \tag{26}$$

where G represents the gradient field. The weighting function $W(k)$ is given as[23]

$$W(k(t)) = \frac{B_1(t)}{\gamma |G(t)|} \tag{27}$$

where $B_1(t)$ is the RF field. The excitation profile can be viewed as the Fourier transform of the product of k-space weighting function and k-space sampling function. In order to avoid aliasing artifacts, a RF pulse is required to create one excitation lobe within the FOV, but this leads to increase in minimum Repetition Time (TR) and hence scan time. On the other hand, short RF pulse leads to excitation profile becoming wider or the excitation profile repeating itself.[23] To overcome this, one can use a shorter RF pulse and in the next step can include removal of the introduced aliasing artifacts using UNFOLD and parallel imaging methods.[23]

UNFOLD is a reconstruction scheme that takes into account the temporal evolution of the signal of every pixel of the image.[72] The idea of UNFOLD technique is that in a dynamic imaging scenario, every pixel in an image has a correlated change observed in the temporal dimension.[72,73] In the dynamic case, maximum signal content tends to appear in the DC component of the frequency domain of the temporal signal. UNFOLD algorithm tries to isolate the DC component from the aliased signal, thereby obtaining the unaliased version of the frequency domain data.[72] Once the filtering operation is done, the image can be obtained by taking the inverse Fourier transform of the unaliased version of the signal.[73]

Parallel imaging involves using multiple receiver coils to collect the data in parallel, thereby reducing the scan time. The reconstruction algorithms involving parallel imaging are SMASH (SiMultaneous Acquisition of Spatial Harmonics)[74] and SENSE (Sensitivity Encoding),[75] with SENSE being widely used due to its fast reconstruction time. In SENSE reconstruction, the distance between the sampling position in k-space is increased while retaining the maximum k-value leading to reduction in scan time.[75] This leads to aliasing due to reduction of sampling density, this aliased image is then used to create the full-FOV image from the set of intermediate images. This is achieved by estimating the signal contribution to each pixel by its neighboring pixels.[75] This kind of signal separation is possible due to the fact that in each single-coil image superposition occurs with different weights according to coil sensitivity.[75] A sensitivity matrix is estimated based on this idea, and this is encoded into the reconstruction procedure. More details about the SENSE algorithm can be found in Preusmann et al.[75]

Above explained schemes can be combined in full/in part to obtain an accurate temperature distribution for MR thermometry. Reduced FOV (rFOV) is imaged and corresponding data is obtained, this results in an aliased signal.[23] The aliased signal can be corrected using parallel imaging and UNFOLD methods.[23,76] Parallel imaging method can be used on aliased signals where there exist a large separation between the main lobe and the smaller side lobes.[23] While UNFOLD can be used to separate regions that are present in close proximity, i.e. can be used to reduced the FWHM of the given Gaussian signal. Usage of these two schemes on the aliased signal results in an unaliased signal.[23] Later, temperature maps can be estimated using this unaliased signal.

3.3 *Temporally Constrained Reconstruction (TCR)*

Another widely used reconstruction method in MR thermometry is by applying a temporal regularization constraint. This method provides acceleration when k-space under sampling pattern is alternated in time. This induces some aliasing artifacts, but those are filtered out by usage of the penalty term (regularization). Temporally Constrained Reconstruction (TCR) is one of the currently available schemes, which has the capability to provide high spatial and temporal resolution along with full three-dimensional coverage, which is essential for performing temperature imaging in MR thermometry. The only drawback of this scheme is that usage of alternating k-space sampling patterns leads to eddy current distortion, and hence limits the acquisition design setup.

The temperature maps are obtained using a temporally constrained reconstruction (TCR), which is based on compressive sensing like approach enforcing the data fidelity and constraining the rapid temporal change. This algorithm draws a parallel to the regularization theory for solving ill-posed inverse problems. The standard discrete inverse Fourier transform reconstruction from the full k-space data can be written as,[21]

$$d = \mathbf{F}m \tag{28}$$

INPUT: $\tilde{d}$ (4-D Undersampled k-space data), W (4-D Sampling Pattern), λ (Regularization Parameter), N_{it} (Number of iterations), st (time frames)
OUTPUT: m (4-D Output Temperature map)

1. Compute the Sliding Window k-space and initial image estimate; $d_{SW} = F'(SW(\tilde{d}. * W))$, $m_{SW} = F'(d_{SW})$; F represents the Fourier Operator, F' represents the Inverse Fourier Operator and SW is the Sliding Window function.
2. Initialize necessary variable; Sparse Image Estimate ($m_{est} = F'(\tilde{d}. * W)$), Image Estimate using SW considering Fourier operator along $1st$ and $3rd$ dimension ($m = F(F(m_{SW}, 1), 3)$)

for i=1 to N_{it}

3. k-space ($\check{d}$) estimate from Image Estimate; $\check{d} = F(m, 2)$
4. Sparse k-space ($\hat{d}$) obtained from Sampling Pattern; $\hat{d} = \check{d}. * W$.
5. Sparse Image Estimate from ($\hat{d}$); $\tilde{m} = F'(\hat{d}, 2)$
6. Gradient of Fidelity Term; $\delta = m_{est} - \tilde{m}$
7. Forward Difference of the Image Estimate; $\triangle m_{fwd}(:,:,:,1:st-1) = m(:,:,:,2:st); \triangle m_{fwd}(:,:,:,st) = m(:,:,:,st)$
8. Backward Difference of the Image Estimate; $\triangle m_{back}(:,:,:,2:st) = m(:,:,:,1:st-1); \triangle m_{back}(:,:,:,1) = m(:,:,:,1)$
9. Temporal Laplacian Estimate; $\Delta^2 m_t = \triangle m_{fwd} - 2 * m + \triangle m_{back}$
10. $\Delta = \delta + \lambda * \Delta^2 m_t$
11. $m = m + \Delta$

end

12. $m = F'(F'(m, 1), 3)$

end

Algorithm 1: Temporally Constrained Reconstruction (TCR).

with d representing the 4-dimensional full data acquired in k-space for various time frames and m (having dimension $M \times N \times$ L $\times P$, where $M \times N \times L$ represents the spatial dimensions corresponding to x, y, and z axis respectively and P represents the temporal dimension) representing the complex image data. Here, **F** represents the Fourier Transform (FT) of each time frame in dynamic sequence taken along the y-dimension. This is considered as the truth and used for comparison with TCR and PICIR algorithm, since full k-space data (without under sampling) is used for reconstruction.

The full k-space data (d) is under sampled, and only sparse data ($\tilde{d}$) is acquired (and the unacquired data points are 0), then the reconstruction can be performed by minimizing the cost functional represented as,[21,24,77]

$$\min_{\tilde{m}} \{\lambda \| (\Delta \tilde{m}) \|_2 + \| \mathbf{WF}\tilde{m} - \tilde{d} \|_2^2\} \tag{29}$$

where **F** is the Fourier transform matrix having a dimension of $N \times N$ (considering along y dimension of the four dimensional data), **W** (of dimension $N \times N$, representation only) is the 4-dimensional binary sparsifying pattern (which represents the phase-encoded lines that are sampled) to obtain $\tilde{d}$ (of dimension $M \times N \times L \times P$) from d (of dimension $M \times N \times L \times P$). The λ is the spatially varying free parameter, and Δ representing the temporal Laplacian. This objective function can now be minimized using a gradient descent approach combined with finite forward difference scheme, leading to a series of image frames updated iteratively as[21]

$$\tilde{m}^{n+1} = \tilde{m}^n - \lambda_s C'(\tilde{m}^n); \quad n = 0, 1, 2, \ldots \tag{30}$$

where λ_s represents the step size corresponding to the gradient descent approach, and $C'(\tilde{m})$ represents the Euler-Lagrange derivative of the objective function given as,[21]

$$C'(\tilde{m}) = 2 * (\mathbf{F}^{-1}(WF\tilde{m}) - \mathbf{F}^{-1}(\tilde{d}) - \lambda \Delta_t^2 \tilde{m}) \tag{31}$$

where Δ_t^2 represents the temporal Laplacian and operates on the complex data. It can be seen that the TCR algorithm takes advantage of Laplacian across frames (previous time point) for performing the temperature map reconstruction. The major steps in the TCR algorithm are given in Algorithm-1. In this review the TCR algorithm with PRF temperature imaging is considered as

standard benchmark to compare the recently developed algorithms.

3.3.1 Advantages of temporally constrained reconstruction algorithm: TCR algorithm provide high spatial resolution and temporal resolution while performing the temperature map reconstruction. TCR algorithm also has the ability to provide reconstruction for large Field of View (FOV). Even though Model Predictive Filtering (MPF) has the ability to provide high spatial and temporal resolution, MPF requires estimation of many parameters like W, Q, ρ, k, and C (all these are tissue dependent). On the other hand, parallel imaging with UNFOLD has good spatial and temporal resolution, but has a limitation of not spanning larger Field of View (FOV), must be restricted to reduced FOV (rFOV) due to usage of 2DRF. Major drawbacks of TCR reconstruction scheme is the eddy currents distortion and lacks the ability to perform real-time temperature imaging. Next section will explain the utility of graphics processing units (GPU) to eliminate the drawback of real-time imaging for TCR method. A real-time TCR (RT-TCR) algorithm that runs on the GPU, having a capability to provide high spatio-temporal resolution with large coverage along with real-time reconstruction (reconstruction is faster than data collection time, making it ideal for MR thermometry). Since TCR is the only method to provide high spatial, temporal and volume coverage, TCR is used for comparison with the PICIR algorithm (discussed later).

4 Real-Time Reconstruction in MR Thermometry

4.1 *Real-Time Temporally Constrained Reconstruction (RT-TCR)*

The original TCR algorithm can be used for performing dynamic three dimensional imaging. In here, the reconstructed image m can be obtained from k-space data, $\tilde{d}$, by iteratively minimizing the cost function:

$$m = arg\min_{m'} \left\{ || WF(m') - \tilde{d} ||_2^2 + \lambda \sum_i^N || \nabla_t m_i' ||_2^2 \right\} \quad (32)$$

where F indicates the Fourier Transform, W indicates which phase encoding lines have to be acquired, m' is the image sequence estimate, and λ is a regularization parameter. Real-time availability of the temperature maps can be achieved using RT-TCR algorithm, for doing this the TCR algorithm is modified in two ways: the TCR code is implemented on Graphics Processing Units (GPU) to reduce the computation time and the algorithm is applied to only a small section of the image matrix around the region of hotspot. Moreover, the estimates for the current temperature map is obtained using only the current and past time frames.[78]

The original TCR algorithm is written in Matlab environment, hence this algorithm was rewritten on the GPU using open-source packages namely CUFFT[79] and CUBLAS[80] provided by CUDA, and are wrapped to make them Matlab executable (mex) files, enabling running of the TCR algorithm on a GPU machine.[78] The RT-TCR algorithm was implemented on a NVIDIA Quadro 6000 GPU machine having 448 cores and 6 GB memory. The data matrix is truncated in x- and z-directions in image space, such that only small ROI around hotspot is reconstructed using RT-TCR algorithm.[78] The remaining region where temperature is static or changes very slowly is reconstructed using sliding window approach to enable faster reconstruction.[78] The most recently acquired k-space data is added to the previous k-space frames in a sliding window fashion, hence enabling data truncation; this data is transformed to image space, truncating the x- and z-directions, and transforming back to k-space.[78] Note that doing truncation in the y-direction is not possible as the undersampling is performed in the phase-encoding direction. This truncated, sliding window k-space is used as the input for the RT-TCR algorithm.

The current time frame in the RT-TCR algorithm is reconstructed based on the current and past information, but also updates that time frame later as and when the future information becomes available.[78] The location of the hotspot and the time frames at which the ultrasound is turned on/off is the only prior information given to the RT-TCR algorithm. To reconstruct the current time frame, t, the RT-TCR algorithm only uses frames $[t - P, t]$, where P is twice the data reduction factor, more detailed illustration is given in Ref. 78. The performance of the RT-TCR algorithm can be seen as the original TCR algorithm to reconstruct a data set with $192 \times 108 \times 30$ image matrix and all 77 time frames, it takes 236 seconds on a 12-core computer with Dual Intel Xeon Processor X5650, 2.66 GHz processing speed, and 64 GB of RAM.[78] The truncated data having a matrix size of $10 \times 108 \times 13$ using the 13 most recent time frame takes around 0.25 seconds using the RT-TCR GPU implementation on an NVIDIA Quadro 6000 with 448 cores. The data transfer from scanner to the computer having GPU card took 0.35 seconds, 0.02 seconds to do the necessary pre-processing

steps, and 0.10 seconds for the post-processing. Note that the total reconstruction time (0.72 seconds) is less than the data acquisition time for one undersampled time frame, thus removing the reconstruction bottleneck.[78] The data reduction along with GPU implementation produced a temperature map reconstruction in 0.72 seconds (including data transfer, running TCR algorithm on GPU, pre- and post-processing steps). Note that RT-TCR it is not faster than Fourier reconstruction, but is faster than one acquisition step, and therefore making it sufficient for the needed temperature feedback.[78]

The implementation of RT-TCR algorithm uses information from previous time frames to improve the image of the current time frame, but if the previous time frames are noisy then the noise will propagate making the estimate inaccurate.[78] Another drawback of RT-TCR is with its inability to handle motion inside the FOV (which is also true for the TCR algorithm), but motion outside the FOV can be handled using the RT-TCR scheme.[78] Despite these drawbacks, the advantage of RT-TCR lies with its ability to provide increased volume coverage without sacrificing spatial or temporal resolution and real-time

INPUT: $\tilde{d}$ (4-D Undersampled k-space data), W (4-D Sampling Pattern), λ (Regularization Parameter), α, N_{it} (Number of iterations), st (time frames)
OUTPUT: m (4-D Output Temperature map)

1. Compute the Sliding Window k-space and initial image estimate; $d_{SW} = F'(SW(\tilde{d}. * W))$, $m_{SW} = F'(d_{SW})$;
2. Initialize necessary variable; Sparse Image Estimate ($m_{est} = F'(\tilde{d}. * W)$), Image Estimate using SW using Fourier operator along $1st$ and $3rd$ dimension ($m = F(F(m_{SW}, 1), 3)$)

for i=1 to N_{it}

3. k-space ($\check{d}$) estimate from Image Estimate; $\check{d} = F(m, 2)$
4. Sparse k-space ($\tilde{d}$) obtained from Sampling Pattern; $\hat{d} = \check{d}. * W$.
5. Sparse Image Estimate from ($\hat{d}$); $\tilde{m} = F'(\hat{d}, 2)$
6. Gradient of Fidelity Term; $\delta = m_{est} - \tilde{m}$
7. Forward Difference of the Image Estimate; $\triangle m_{fwd}(:,:,:,1:st-1) = m(:,:,:,2:st); \triangle m_{fwd}(:,:,:,st) = m(:,:,:,st)$
8. Backward Difference of the Image Estimate; $\triangle m_{back}(:,:,:,2:st) = m(:,:,:,1:st-1); \triangle m_{back}(:,:,:,1) = m(:,:,:,1)$
9. Temporal Laplacian Estimate; $\Delta^2 m_t = \triangle m_{fwd} - 2 * m + \triangle m_{back}$

for $t = 1$ to st
if $t < \frac{st}{2}$
if $t == 1$

10. $m_{pr}(:,:,:,1) = m(:,:,:,1)$

else

11. $m_{pr}(:,:,:,t) = m(:,:,:,t-1)$

end
else
if $t == st$

12. $m_{pr}(:,:,:,t) = m(:,:,:,t)$

else

13. $m_{pr}(:,:,:,t) = m(:,:,:,t+1)$

end
end

14. $\triangle m_{pr} = m - m_{pr}$; $\Delta = \delta + (1-\alpha) * \lambda * \Delta^2 m_t + \alpha * \lambda * \triangle m_{pr}$; $m = m + \Delta$

end

15. $m = F'(F'(m, 1), 3)$

end

Algorithm 2: Prior Image Constrained Image Reconstruction (PICIR).

reconstruction, making it suitable for monitoring temperature changes.

4.2 *Prior Image Constrained Image Reconstruction (PICIR)*

Another approach for achieving real-time reconstruction is by reducing the scan time, i.e. acquiring less number of measurements, without compromising the quality of the reconstructed temperature maps. At present, the TCR algorithm provides reasonably accurate reconstruction with 2–8 reduction factor in the data, higher reduction factor is desirable (resulting in faster scan time). TCR applied a temporal constrain to perform the image reconstruction, while in PICIR algorithm an extra term is added as a constraint involving the previous or the next time frame. The accuracy of the temperature map reconstruction can be improved by using the PICIR framework, where the minimization of the unconstrained variant is considered, namely[31,32]

$$\min_{\tilde{m}}\{\lambda[\alpha||(\tilde{m}-\tilde{m}_{pr})||_2^2+(1-\alpha)||(\Delta\tilde{m})||_2^2 + ||\tilde{\mathrm{F}}\tilde{m}-\tilde{d}r||_2^2\} \quad (33)$$

with λ representing the non-negative regularization parameter and $\tilde{m}_{pr}$ being the prior information obtained as the previous or the next time frame. The prior image is defined as,

$$\tilde{m}_{pr}=\begin{cases}\tilde{m}_{i+1} & if\ i>\dfrac{P}{2},\\ \tilde{m}_{i-1} & if\ i>\dfrac{P}{2}.\end{cases} \quad (34)$$

where P represents the total number of time frames.

Here when the temperature is rising the previous time frame should act as prior reference and for the falling temperatures the next time frame should act as prior reference. It is important to note that the first time point reconstruction is performed by having fully sampled k-space data, the next time points have sampled version of the k-space data, which is similar to the TCR algorithm. The weight factor is represented by α ($\alpha = 1$ indicates full weight for the prior and $\alpha = 0$ indicates reconstruction performed using the TCR approach).

Solving of Eq. (33) can be done using a gradient descent approach with finite forward difference, leading to a series of image frames updated iteratively as

$$\tilde{m}^{n+1}=\tilde{m}^{n}-\lambda_s C(\tilde{m}^{n}); \quad n=0,1,2,\ldots \quad (35)$$

where λ_s represents the step size corresponding to the gradient descent approach, and $C(\tilde{m})$ represents the Euler-Lagrange derivative of the objective function given as,[21]

$$C(\tilde{m})=2*(\mathrm{F}^{-1}(\mathrm{WF}\tilde{m})-\mathrm{F}^{-1}(\tilde{d}) -\lambda((1-\alpha)*\Delta_t^2\tilde{m})-\lambda(\alpha*(\tilde{m}-\tilde{m}_{pr}))) \quad (36)$$

The major steps of PICIR algorithm for the 4-D temperature map reconstruction are indicated in Algorithm-2. The inclusion of this prior term into the minimization helps in performing the reconstruction with very less measurements compared to the standard TCR algorithm. It is important to note that in both the TCR and PICIR algorithms, the sliding window reconstruction is used as the initial image estimate (current TCR works in this fashion). The comparison of this scheme (PICIR algorithm) is performed using *ex vivo* pork muscle experiments, which will discussed in the next section.

5 Simulations and Results

5.1 *Simulation and experiments*

The PICIR method was evaluated using MRgHIFU data sets. The HIFU heating were performed in a Siemens TIM Trio MRI scanner (Siemens Medical Solutions, Erlangen, Germany) using an MRI-compatible phased array transducer (13 cm radius of curvature, 256 elements, 1 MHz frequency, Imasonic, Besancon, France and Image Guided Therapy, Pessac, France). Imaging for all experiments was done with a 3D segmented EPI gradient echo sequence.[78]

In the first set of experiments, HIFU heating experiments were performed on an *ex vivo* pork muscle sample at 36 Acoustic watts for 30 seconds. The rate of change in temperature at this power level was 2.2°C/s.[78] At this power level, the heating was repeated twice under identical circumstances. In the first instance, imaging parameters were chosen such that the 3D volume could be fully sampled at adequate temporal resolution. These fully sampled data sets were reconstructed with the standard Fourier Transform approach and used to compute temperature maps that was considered as truth. Imaging parameters for the fully sampled data were: 128 × 72 × 12 imaging matrix (10 slices plus 20% slice oversampling), 1.5 × 1.5 × 3.0 mm resolution, TE = 10 ms, TR = 25 ms, EPI Factor = 9, flip angle = 20°, bandwidth = 738 Hz/pixel, 2.4 seconds per scan. Then the PICIR and TCR reconstruction methods were run by under sampling the acquired fully sampled data, the

reconstruction was performed by sampling only 33% and 16% of fully-sampled data acquired from the MRI scanner.

The TCR and PICIR temperature map estimation was done for larger 3D volumes that were acquired at an under sampling factor of 6X.[78] Each pair of identical heating runs was performed at the same location in the sample. Imaging parameters for the under sampled data were: 1.5 × 1.5 × 3.0 mm resolution, 128 × 108 × 24 imaging matrix (22 slices plus 9% slice oversampling), TR = 25 ms, TE = 10 ms, EPI Factor = 9, flip angle = 20°, bandwidth = 738 Hz/pixel, 6X under sampling, 1.2 seconds per under sampled time frame.[78] This under sampled data was used to obtain the temperature maps with TCR and PICIR algorithms, and then compared with the standard Fourier transform reconstruction performed with full data. The obtained 6X undersampled dataset was further undersampled by 50% and the reconstruction was performed using this highly undersampled data. The undersampled data was used to show the efficacy of the PICIR approach to reconstruct the temperature maps more accurately compared to the traditional TCR approach at higher reduction rates.

The PICIR scheme was also evaluated with noise levels using the 6X data. Hence, a zero-mean Gaussian random noise was added to the undersampled k-space data such that the sliding window reconstruction of the noisy k-space produced a temperature maps with temperature standard deviations of 1.02°C as measured over the region of interest (ROI). This noisy data was used to perform the reconstruction using the TCR and the PICIR approach. The obtained noisy data was further undersampled by 50% and the reconstruction was performed to show the effectiveness of the PICIR scheme with less measurements. The image reconstruction procedure was carried out on an machine having Intel Xeon dual six core processor with a processor speed of 2.66 GHz and memory of 64 GB.

5.2 *Results*

The fully sampled data obtained from the MRI scanner was undersampled to have only 33% and 16% of the data. This data was used for estimating the temperature maps using TCR and PICIR method. The temperature map reconstruction, and difference between the reconstructed temperature maps with the truth (reconstructed with Fourier transform approach having full data) is shown in Fig. 1. It can be clearly seen that the PICIR scheme performs better at estimation of the temperature when compared to the TCR algorithm when the available data is very less. The weight parameter α was kept as 0.3 in all cases. The computational time along with the Root Mean Square Error (RMSE) is reported in Table 1. The RMSE was calculated for 5 × 5 × 7 voxel in the region of interest over all the time points as used in Ref. 24. The gradient

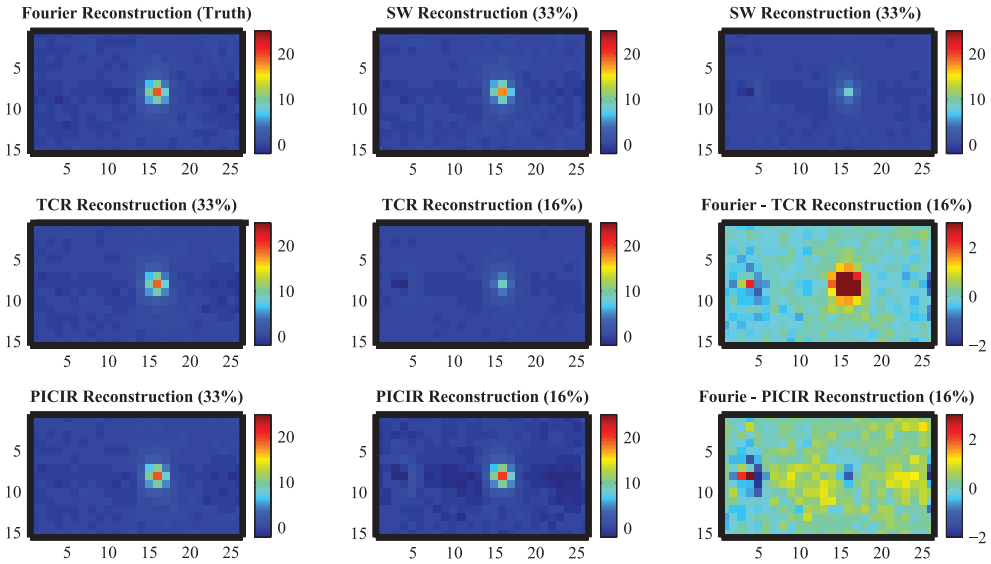

Figure 1: Comparison of temperature map reconstruction of the standard Temporally Constrained Reconstruction (TCR) with Prior Image Constrained Image Reconstruction (PICIR) method. The reconstruction was performed using 33% and 16% of the acquired Fully-sampled data. Difference image is also shown for better comparison of reconstructed temperature distribution. Sliding Window (SW) reconstruction is also incuded for completion.

Table 1: Comparison of computational time and root mean square error for the results presented in this work.

	Fully Sampled Data (Fig. 1)				Undersampled Data (Fig. 2)			
Method	TCR (33%)	TCR (16%)	PICIR (33%)	PICIR (16%)	TCR (17%)	TCR (8.5%)	PICIR (17%)	PICIR (8.5%)
Data Acquisition Time	1	0.5	1	0.5	1	0.5	1	0.5
Reconstruction Time (time in seconds)	1 (6.67)	1 (7.39)	1.66 (11.104)	1.57 (11.65)	1 (55.62)	1 (54.32)	1.61 (89.86)	1.63 (88.48)
Total Time	2	1.5	2.66	2.07	2	1.5	2.61	2.13
RMSE	0.235	2.815	0.242	0.784	0.42	1.24	0.43	0.56

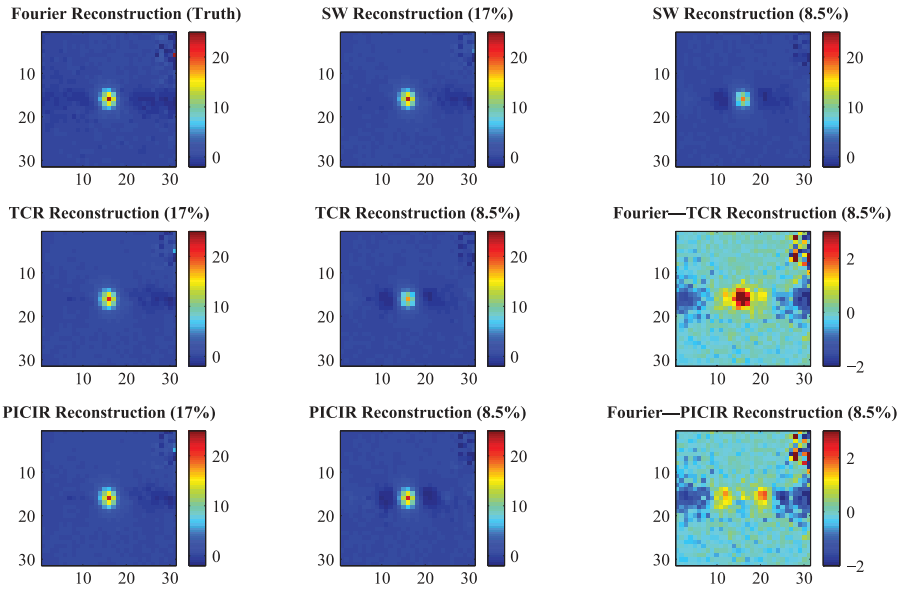

Figure 2: Comparison of temperature map reconstruction of the standard Temporally Constrained Reconstruction (TCR) with Prior Image Constrained Image Reconstruction (PICIR) method. The sampling used is shown in the parenthesis. Difference image is also shown for better comparison of reconstructed temperature distribution. Sliding Window reconstruction is also included for completion.

descent algorithm was run for 100 iterations in all the cases. The reconstruction parameter λ was set to 0.05 for all the noiseless cases considered here and 0.001 for higher noise case.

The reconstructed temperature maps using the 6X under sampled data obtained from the MRI scanner for the TCR and PICIR algorithms are shown in Fig. 2. This data was further undersampled by 50%, and the reconstruction results pertaining to this data set along with the difference between the reconstructed temperature maps and the truth is shown in Fig. 2. The temperature map distribution in Fig. 2 shows that both TCR and PICIR results in a similar reconstruction when the 6X undersampled data was used, while PICIR outperforms TCR with lesser measurements (12X). Hence, it can be clearly concluded that PICIR algorithm works well with highly undersampled data cases, the same was observed from the RMSE values given in Table 1.

To show the effectiveness of the PICIR scheme in noisy environment with less measurements, the obtained under sampled MRI data (6X undersampling) was added with noise. The resultant noisy data was undersampled by 50%, and then temperature map was reconstructed using TCR and PICIR method using this highly under sampled data. The reconstruction distribution using 17% and 8.5% measurements is shown in Fig. 3. The reconstruction indicates that the PICIR scheme being robust with noise, is able to reconstruct the temperature distribution more accurately compared to the TCR algorithm with fairly less measurements, leading to faster data collection. In all the above cases, the sliding window reconstruction is also included for the sake of completion.

5.3 *Discussion*

The performance of the PICIR method for the obtained sampled MRgHIFU dataset was

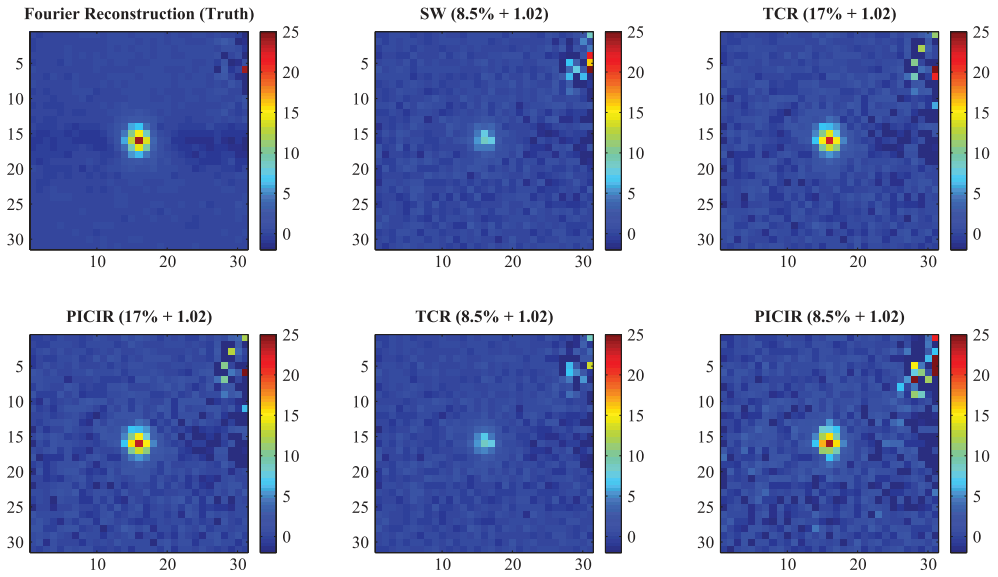

Figure 3: Similar effort as the previous case, here testing of the performance of reconstruction was done with noisy data. The percentage of sampling and noise (in °C) used is indicated in parenthesis.

observed to be superior compared to the standard TCR approach (see Figs 1, 2 and 3). It is important to note that the TCR performance is similar to the PICIR algorithm for cases where number of measurements available is high (factor of reduction below 12). Since the number of measurements required are less for PICIR, the data-collection time is be faster. It is important to note that the same data sets were used for obtaining the temperature maps for both TCR and PICIR algorithms. PICIR method was also evaluated using noisy measurements (noise introduced by the coil) and was observed that even at higher noise levels PICIR method was able to reconstruct the temperature maps more accurately compared to the TCR algorithm with less number of measurements. As prior image provides a robust support for the reconstruction in case of sparse data, the temperature maps obtained through PICIR were more accurate compare to the TCR results.

Table 1 indicates the time taken for the reconstruction of temperature maps using the TCR approach and the proposed method. The reported time in Table 1 indicates that the PICIR method is computationally expensive when compared to the TCR algorithm. But, since PICIR was able to give reasonable RMSE values (less than 1°C at the ROI) when less measurements are acquired as shown in Table 1. Hence assuming that the data-collection time is within the same scale as the reconstruction time, it can be concluded that PICIR algorithm can be used as a alternative to the TCR algorithm when the number of measurement available are fairly low, the same has been emphasized in Table 1. As a part of future work, the PICIR algorithm would be rewritten for achieving massive parallelism using GPUs.

One limitation of the PICIR algorithm is that it has two reconstruction parameters (α and λ) compared to the TCR algorithm (which has only λ) to be chosen. Choice of these reconstruction parameters will largely influence the accuracy of the reconstructed temperature distribution, which is well studied in the inverse problems literature. Even though PICIR algorithm requires multiple parameters, it was observed that the PICIR algorithm was fairly stable for the choice of the reconstruction parameters in similar lines as that of TCR.[24] It is important to note that PICIR kind of algorithm is widely used in the tomography literature, where it was also shown to stable in terms of reconstruction parameters.

The discussed methods are able to handle motion outside the region of interest, but these algorithms are not poised to handle motion in the region of interest. A recent study showed a real-time in-plane motion correction to permit both temperature and thermal-dose calculations on the fly, the same was evaluated to handle motion in abdominal organs.[81] Recent work has also tried to evaluate a real-time Proton Resonant Frequency (PRF) based MR thermometry with a novel motion compensation technique, using linear phase model and active tracking coils.[82] Hence, incorporating motion estimation and correction into the reconstruction procedure with the help of inverse problems needs to be addressed.

6 Conclusion and Future Work

In conclusion, this paper aimed at reviewing the available temperature reconstruction methods for performing MR thermometry. As the recent focus in MR thermometry has been on obtaining real-time temperature reconstruction for large volume of interest, two such methods TCR and PICIR are discussed here. Through ex-vivo studies, it was established that PICIR approach, which uses prior image as a constrain was able to provide more accurate temperature map distribution with fewer measurements when compared to the existing TCR approach. Also the PICIR method was able to provide high spatio-temporal resolution and volume coverage with relatively lesser measurements (thereby reducing the scan time). RT-TCR algorithm was able to provide increased volume coverage without sacrificing spatial or temporal resolution, and real-time reconstruction making it suitable for monitoring temperature changes.

Further, recent works on dynamic MRI imaging introduced an algorithm called *MotionTV*,[85] was shown to perform better than the traditional total variation and l_1-norm based image reconstruction. Therefore, a future study focussing on comparing all the algorithms including TCR, PICIR and *MotionTV*[85] based reconstruction of temperature maps in MRgHIFU, which can provide better understanding with the utility of these reconstruction schemes is necessary. The usage of prior information in the l_1-norm and l_0-norm[83,84] based framework will be taken up in the future. In general, the future work could be pursued in combining the various MR parameters for estimating the temperature distribution in MR thermometry.

Acknowledgment

The authors would like to acknowledge Manish Bhatt for proof-reading the manuscript. This work is supported by Department of Biotechnology (DBT) Rapid Grant for Young investigator (RGYI) (No: BT/PR6494/GDB/27/415/2012) and DBT Bioengineering Grant (No:BT/PR7994/MED/32/284/2013). JP acknowledges the support by Microsoft Corporation and Microsoft Research India under the Microsoft Research India PhD Fellowship Award and SPIE Optics and Photonics Education Scholarship.

Received 7 June 2014.

References

1. K. Hynynen, C. Damianou, A. Darkazanli, E. Unger, and J.F. Schenck, "The feasibility of using MRI to monitor and guide noninvasive ultrasound surgery," Ultrasound Med. Biol. **19**, 91–92 (1993).
2. B.D. de Senneville, B. Quesson, and C.T.W. Moonen, "Magnetic resonance temperature imaging," Int. J. Hypertherm. **21**, 515–531 (2005).
3. M.G. Mack, R. Straub, K. Eichler, K. Engelmann, S. Zangos, A. Roggan, D. Woitaschek, M. Bottger, and T.J. Vogl, "Percutaneous MR imaging-guided laser-induced thermotherapy of hepatic metastases," Abdom. Imaging. **26**, 369–374 (2001).
4. S. Thomsen, "Pathologic analysis of photothermal and photomechanical effects of laser-tissue interactions," Photochem. Photobiol. **53**, 825–835 (1991).
5. R.J. Stafford, D. Fuentes, A.A. Elliott, J.S. Weinberg, and K. Ahrar, "Laser-induced thermal therapy for tumor ablation," Crit. Rev. Biomed. Eng. **38**, 79–100 (2010).
6. P. P. Lele, "Production of deep focal lesions by focused ultrasound current status," Ultrasonics **5**, 105–112 (1967).
7. K. Hynynen, N. McDannold, G. Clement, F.A. Jolesz, E. Zadicario, R. Killiany, T. Moore, and D. Rosen, "Pre-clinical testing of a phased array ultrasound system for MRI-guided noninvasive surgery of the brain primate study," Eur. J. Radiol. **59**, 149–156 (2006).
8. S. L. Hokland, M. Pedersen, R. Salomir, B. Quesson, H. Stodkilde-Jorgensen, and C.T.W. Moonen, "MRI-guided focused ultrasound: Methodology and applications," IEEE Trans. Med. Imaging. **25**, 723–731 (2006).
9. V. Chan and A. Perlas, "Basics of Ultrasound Imaging," Springer DOI 10.1007/978-1-4419-1681-5-2.
10. C.A. Speed, "Therapeutic ultrasound in soft tissue lesions," Rheum. **40**, 1331–1336 (2001).
11. P.A. Artho, J.G. Thyne, B.P. Warring, C.D. Willis, J.M. Brismee, and N.S. Latman, "A Calibration Study of Therapeutic Ultrasound Units," Phys. Ther. **82**, 257–263 (2002).
12. N. Bloembergen, E.M. Purcell, and R.V. Pound, "Relaxation effects in nuclear magnetic resonance absorption," Physical Review. **73**, 679–712 (1948).
13. J. Hindman, "Proton resonance shift of water in the gas and liquid states," J. Chem. Phys. **44**, 4582–4592 (1966).
14. D.L. Parker, "Applications of NMR imaging in hyperthermia: An evaluation of the potential for localized tissue heating and noninvasive temperature monitoring," IEEE Trans. Biomed. Eng. **31**, 161–167 (1984).
15. D.L. Parker, V. Smith, P. Sheldon, L.E. Crooks, and L. Fussell, "Temperature distribution measurements in two-dimensional NMR imaging," Med. Phys. **10**, 321–325 (1983).
16. Y. Ishihara, A. Calderon, H. Watanabe, K. Okamoto, Y. Suzuki, K. Kuroda, and Y. Suzuki, "A precise and fast temperature mapping using water proton chemical shift," Magn. Reson. Med. **34**, 814–823 (1995).
17. J.D. Poorter, C.D. Wagter, Y.D. Deene, C. Thomsen, F. Stahlberg, and E. Achten, "Noninvasive MRI thermometry with the proton resonance frequency (PRF) method: In vivo results in human muscle," Magn. Reson. Med. **33**, 74–81 (1995).

18. J.D. Poorter, "Noninvasive MRI thermometry with the proton resonance frequency method: Study of susceptibility effects," Magn. Reson. Med. **34**, 359–367 (1995).
19. Y. Huang, J. Song, and K. Hynynen, "MRI monitoring of skull-base heating in transcranial focused ultrasound ablation," Proc. of ISMRM 249, (2010).
20. C. Mougenot, M.O. Kohler, J. Enholm J, B. Quesson, and C. Moonen, "Quantification of near-field heating during volumetric MR-HIFU ablation," Med. Phys. **38**, 272–282 (2011).
21. G. Adluru, S.P. Awate, T. Tasdizen, R.T. Whitaker, and E.V. Dibella, "Temporally constrained reconstruction of dynamic cardiac perfusion MRI," Magn. Reson. Med. **57**, 1027–1036 (2007).
22. N. Todd, A. Payne, and D.L. Parker, "Model predictive filtering for improved temporal resolution in MRI temperature imaging," Magn. Reson. Med. **63**, 1269–1279 (2010).
23. C.S. Mei, L. P. Panych, J. Yuan, N.J. McDannold, L.H. Treat, Y. Jing, and B. Madore, "Combining two-dimensional spatially selective RF excitation, parallel imaging, and UNFOLD for accelerated MR thermometry imaging," Magn. Reson. Med. **66**, 112–122 (2011).
24. N. Todd, U. Vyas, J. de Bever, A. Payne, and D.L. Parker, "Reconstruction of fully three-dimensional high spatial and temporal resolution MR temperature maps for retrospective applications," Magn. Reson. Med. **67**, 724–730 (2012).
25. G. Pratx and L. Xing, "GPU computing in medical physics: A review," Med. Phys. **38**, 2685–2697 (2011).
26. T. Schiwietz, T.C. Chang, P. Speier, and R. Westermann, "MR image reconstruction using the GPU," Proc. of SPIE 6142, (2006).
27. T. Sorensen, D. Atkinson, T. Schaeffter, and M. Hansen, "Real-time reconstruction of sensitivity encoded radial magnetic resonance imaging using a graphics processing unit," IEEE Trans. Med. Imaging **28**, 1974–1985 (2009).
28. J. Prakash, V. Chandrasekharan, V. Upendra, and P.K. Yalavarthy, "Accelerating frequency-domain diffuse optical tomographic image reconstruction using graphics processing units," J. Biomed. Opt. **15**, 066009 (2010).
29. B. Zhang, X. Yang, F. Yang, X. Yang, C. Qin, D. Han, X. Ma, K. Liu, and J. Tian, "The CUBLAS and CULA based gpu acceleration of adaptive finite element framework for bioluminescence tomography," Opt. Exp. **18**, 20201–20214 (2010).
30. M. Freiberger, F. Knoll, K. Bredies, H. Scharfetter, and R. Stollberger, "The AGILE library for image reconstruction in biomedical sciences using graphics card hardware acceleration," Computing in Science and Engg. **15**, 34–44 (2013).
31. G.H. Chen, J. Tang, and S. Leng, "Prior image constrained compressed sensing (PICCS): A method to accurately reconstruct dynamic CT images from highly undersampled projection data sets," Med. Phys. **35**, 660–663 (2008).
32. G.H. Chen, J. Tang, and J. Hsieh, "Temporal resolution improvement using PICCS in MDCT cardiac imaging," Med. Phys. **36**, 2130–2135 (2009).
33. P.A. Bottomley, T.H. Foster, R.E. Argersinger, and L.M. Pfeifer, "A review of normal tissue hydrogen NMR relaxation times and relaxation mechanisms from 1–100 MHz: dependence on tissue type, NMR frequency, temperature, species, excision, and age," Med. Phys. **11**, 425–448 (1984).
34. H.E. Cline, J.F. Schenck, R.D. Watkins, K. Hynynen, and F.A. Jolesz, "Magnetic resonance-guided thermal surgery," Magn. Reson. Med. **30**, 98–106 (1993).
35. C.J. Lewa and Z. Ma Jewska, "Temperature relationships of proton spin-lattice relaxation time T1 in biological tissues," Bull Cancer. **67**, 525–530 (1980).
36. H.E. Cline, K. Hynynen, C.J. Hardy, R.D. Watkins, J.F. Schenck, and F.A. Jolesz, "MR temperature mapping of focused ultrasound surgery," Magn. Reson. Med. **31**, 628–636 (1994).
37. K. Hynynen, N. McDannold, R.V. Mulkern, and F. A. Jolesz, "Temperature monitoring in fat with MRI," Magn. Reson. Med. **43**, 901–904 (2000).
38. R. Matsumoto, K. Oshio, and F.A. Jolesz, "Monitoring of laser and freezing-induced ablation in the liver with T1-weighted MR imaging," J. Magn. Reson. Imaging. **2**, 555–562 (1992).
39. V. Rieke and K.B. Pauly, "MR Thermometry," J. Magn. Reson. Imaging. **27**, 376–390 (2008).
40. T.R. Nelson and S.M. Tung, "Temperature dependence of proton relaxation times in vitro," Magn. Reson. Imaging. **5**, 189–199 (1987).
41. M. Peller, H.M. Reinl, A. Weigel, M. Meininger, R.D. Issels, and M. Reiser, "T1 relaxation time at 0.2 Tesla for monitoring regional hyperthermia: feasibility study in muscle and adipose tissue," Magn. Reson. Med. **47**, 1194–1201 (2002).
42. T.J. Vogl, R. Straub, S. Zangos, M.G. Mack, and K. Eichler, "MR-guided laser-induced thermotherapy (LITT) of liver tumors: Experimental and clinical data," Int. J. Hyperthermia. **20**, 713–724 (2004).
43. D. Freude, "Spectroscopy: Lecture on Nuclear Magnetic Resonance," University of Leipzig (2004).
44. P.T. Vesanen, K.C.J. Zevenhoven, J.O. Nieminen, J. Dabek, L.T. Parkkonen, and R.J. Ilmoniemi, "Temperature dependence of relaxation times and temperature mapping in ultra-low-field MRI," J. Magn. Reson. **235**, 50–57 (2013).
45. S.J. Graham, M.J. Bronskill MJ, and R.M. Henkelman, "Time and temperature dependence of MR parameters during thermal coagulation of ex vivo rabbit muscle," Magn. Reson. Med. **39**, 198–203 (1998).
46. S. Gandhi, B.L. Daniel, and K.B. Pauly, "Temperature dependence of relaxation times in bovine adipose tissue," Proc. Intl. Soc. Mag. Reson. Med. 701, (1998).
47. A. Abragam, "The principles of nuclear magnetism," Chapter I. Oxford: The Claredon Press (1983).
48. F. Johnson, H. Eyring, and B. Stover, "Theory of rate processes in biology and medicine," New York: John Wiley & Sons (1974).

49. J. Chen, B.L. Daniel, and K.B. Pauly, "Investigation of proton density for measuring tissue temperature," J. Magn. Reson. Imaging. **23**, 430–434 (2006).
50. D.H. Gultekin and J.C. Gore, "Temperature dependence of nuclear magnetization and relaxation," J. Magn. Reson. **172**, 133–141 (2005).
51. R. Catane, A. Beck, Y. Inbar, T. Rabin, N. Shabshin, S. Hengst, R.M. Pfeffer, A. Hanannel, O. Dogadkin, B. Liberman, and D. Kopelman, "MR-guided focused ultrasound surgery (MRgFUS) for the palliation of pain in patients with bone metastases preliminary clinical experience," Ann. Oncology, **18**, 163–167 (2006).
52. J. Chen, B.L. Daniel, J.M. Pauly, and K.B. Pauly, "Observations on the Temperature Dependence of Apparent Proton Density in Bovine Adipose and Muscle," Proc. Intl. Soc. Mag. Reson. Med. (2003).
53. D.L. Bihan, J. Delannoy, and R.L. Levin, "Temperature mapping with MR imaging of molecular diffusion: Application to hyperthermia," Radiology. **171**, 853–857 (1989).
54. E.O. Stejskal and J.E. Tanner, "Spin diffusion measurements—spin echoes in presence of a time-dependent field gradient," J. Chem. Phys. **42**, 288–292 (1965).
55. A.R. Bleier, F.A. Jolesz, M.S. Cohen, R.M. Weisskoff, J.J. Dalcanton, N. Higuchi, D.A. Feinberg, B.R. Rosen, R.C. McKinstry, and S.G. Hushek, "Real-time magnetic resonance imaging of laser heat deposition in tissue," Magn. Reson. Med. **21**, 132–139 (1991).
56. D. Morvan, A. Leroy-Willig, A. Malgouyres, C.A. Cuenod, P. Jehenson, and A. Syrota, "Simultaneous temperature and regional blood volume measurements in human muscle using an MRI fast diffusion technique," Magn. Reson. Med. **29**, 371–377 (1993).
57. M.E. Moseley, Y. Cohen, J. Mintorovitch, L. Chileuitt, H. Shimizu, J. Kucharczyk, M.F. Wendland, and P.R. Weinstein, "Early detection of regional cerebral ischemia in cats: Comparison of diffusion- and T2-weighted MRI and spectroscopy," Magn. Reson. Med. **14**, 330–346 (1990).
58. J. MacFall, D.M. Prescott, E. Fullar, and T.V. Samulski, "Temperature dependence of canine brain tissue diffusion coefficient measured in vivo with magnetic resonance echo-planar imaging," Int. J. Hyperthermia. **11**, 73–86 (1995).
59. G. Nemethy and H. Scheraga, "Structure of water and hydrophobic bonding in proteins. 1. A model for thermodynamic properties of liquid water," J. Chem. Phys. **36**, 3382–3392 (1962).
60. W.G. Schneider, H.J. Bernstein, and J.A. Pople, "Proton magnetic resonance chemical shift of free (gaseous) and associated (liquid) hydride molecules," J. Chem. Phys. **28**, 601–607 (1958).
61. E.B. Cady, P.C. D'Souza, J. Penrice, and A. Lorek, "The estimation of local brain temperature by in vivo 1H magnetic resonance spectroscopy," Magn. Reson. Med. **33**, 862–867 (1995).
62. I. Marshall, B. Karaszewski, J.M. Wardlaw, V. Cvoro, K. Wartolowska, P.A. Armitage, T. Carpenter, M.E. Bastin, A. Farrall, and K. Haga, "Measurement of regional brain temperature using proton spectroscopic imaging: Validation and application to acute ischemic stroke," Magn. Reson. Imaging. **24**, 699–706 (2006).
63. K. Kuroda, R.V. Mulkern, K. Oshio, L.P. Panych, T. Nakai, T. Moriya, S. Okuda, K. Hynynen, and F.A. Jolesz, "Temperature mapping using the water proton chemical shift: Self-referenced method with echo-planar spectroscopic imaging," Magn. Reson. Med. **43**, 220–225 (2000).
64. K. Kurodat, "Non-invasive MR thermography using the water proton chemical shift," Int. J. Hyperthermia. **21**, 547–560 (2005).
65. D.J. Drost, W.R. Riddle, and G.D. Clarke, "Proton magnetic resonance spectroscopy in the brain: Report of AAPM MR Task Group #9," Med. Phys. **29**, 2177 (2002).
66. J. Parikh, "Measurement of brain temperature using magnetic resonance spectroscopic imaging," Doctoral Thesis, University of Edinburgh (2013).
67. H.E. Cline, K. Hynynen, E. Schneider, C.J. Hardy, S.E. Maier, R.D. Watkins, and F.A. Jolesz, "Simultaneous magnetic resonance phase and magnitude temperature maps in muscle," Magn. Reson. Med. **35**, 309–315 (1996).
68. N. Todd, "Improved magnetic resonance temperature imaging through pulse sequence and reconstruction techniques," Doctoral Dissertation, University of Utah (2013).
69. N. McDonnold, F.A. Jolesz, and K. Hynynen, "Determination of the optimal delay between sonifications during focused ultrasound surery in rabbits by using MR imaging to monitor thermal build up in vivo," Radiology. **211**, 419–426 (1999).
70. N. McDonnold, K. Hynynen, D. Wolf, G. Wolf, and F.A. Jolesz, "MRI evaluation of thermal ablation of tumors with focused ultrasound," J. Magn. Reson. Imaging. **8**, 91–100 (1998).
71. J. Pauly, D. Nishimura, and A. Macovski, "A K-Space Analysis of Small-Tip-Angle Excitation," J. Magn. Reson. **81**, 43–56 (1989).
72. B. Madore, G.H. Glover, and N.J. Pelc, "Unaliasing by Fourier-encoding the overlaps using the temporal dimension (UNFOLD), applied to cardiac imaging and fMRI," Magn. Reson. Med. **42**, 813–828 (1999).
73. B. Madore, "Using UNFOLD to remove artifacts in parallel imaging and in partial-Fourier imaging," Magn. Reson. Med. **48**, 493–501 (2002).
74. D.K. Sodickson and W.J. Manning, "Simultaneous acquisition of spatial harmonics (SMASH): Fast imaging with radiofrequency coil arrays," Magn. Reson. Med. **38**, 591–603 (1997).
75. K.P. Pruessmann, M. Weiger, M.B. Scheidegger, and P. Boesiger, "SENSE: Sensitivity encoding for fast MRI," Magn. Reson. Med. **42**, 952–962 (1999).
76. B. Madore, "UNFOLD-SENSE: A parallel MRI method with self-calibration and artefact suppression," Magn. Reson. Med. **52**, 310–320 (2004).
77. N. Todd, G. Adluru, E. V. R. Dibella, and D. Parker, "Temporally constrained reconstruction applied to MRI temperature data," Magn. Reson. Med. **62**, 406–419 (2009).

78. N. Todd, J. Prakash, H. Oden, J.d. Bever, A. Payne, P.K. Yalavarthy, and D.L. Parker, "Towards real-time availability of 3-D temperature maps created with tempo-rally constrained reconstruction," Magn. Reson. Med. **71**, 1394–1404 (2014).
79. Weblink: *http://www.dms.umontreal.ca/math/GPU/documents/CUFFT_Library_3.0.pdf* (accessed on 22 December 2012).
80. Weblink: *http://docs.nvidia.com/cuda/pdf/CUDA_CUBLAS_Users_Guide.pdf* (accessed on 22 December 2012).
81. B. D. de Senneville, S. Roujol, C. Moonen, and M. Ries, "Motion correction in MR thermometry of abdominal organs: a comparison of the referenceless vs. the multibaseline approach," Magn. Reson. Med. **64**, 1373–1381 (2010).
82. P. Wang and O. Unal, "Motion-compensated real-time MR thermometry augmented by tracking coils," J. Magn. Reson. Imaging. (2014), DOI: 10.1002/jmri.24574.
83. W. A. Grissom, V. Rieke, A. B. Holbrook, Y. Medan, M. Lustig, J. Santos, M. V. McConnell, and K. B. Pauly, "Hybrid referenceless and multibaseline subtraction MR thermometry for monitoring thermal therapies in moving organs," Med. Phys. **37**, 5014–5026 (2010).
84. P. Gaur and W. A. Grisson, "Direct reconstruction of proton resonance frequency-shift temperature maps from k-space data for highly-accelerated thermometry," Proc. of ISMRM (2013).
85. C. Bilen, I. Selesnick, Y. Wang, R. Otazo, and D. K. Sodickson, "A Motion Compensating Prior for Dynamic MRI Reconstruction using Combination of Compressed Sensing and Parallel Imaging," IEEE Signal Processing in Medicine and Biology Symposium (SPMB) 1–6 (2011).

Jaya Prakash received the B.Tech. degree in Information Technology from the Amrita School of Engineering, Bangalore, India, in 2010, and the M.Sc. [Engg.] degree in Supercomputer Education and Research Centre (SERC) from the Indian Institute of Science, Bangalore, India, in November 2012, where he is currently working towards the Ph.D. degree in medical imaging. He was the coauthor of the paper chosen for ISMRM Merit Award (Summa Cum Laude) in 2012. He is the recipient of SPIE Optics and Photonics Education Scholarship and Microsoft Research Indian PhD Fellowship in 2013. His research interests include biomedical optical imaging, compressive sensing, GPU computing, and inverse problems in medical imaging.

Nick Todd is a senior research associate at the University College London. Earlier, he worked as a post-doctoral research associate in the Radiology department at the University of Utah in Salt Lake City, Utah. He earned his Ph.D. from the Physics Department at the University of Utah in 2010 under the mentorship of Prof. Dennis L. Parker. His research has focused on improving Magnetic Resonance Imaging (MRI) techniques for temperature mapping, with a particular focus on High Intensity Focused Ultrasound (HIFU) applications.

Phaneendra K. Yalavarthy is an assistant professor in Supercomputer Education and Research Centre at Indian Institute of Science, Bangalore. He received Ph.D. degree in biomedical computation from Dartmouth College in 2007 and holds a M.Sc. degree in Engineering from Indian Institute of Science, Bangalore. His research interests include medical image computing, medical image analysis, and biomedical optics.